

HW/SW Co-design for Reliable TCAM-based In-memory Brain-inspired Hyperdimensional Computing

Simon Thomann, *Member, IEEE*, Paul R. Gessler, *Member, IEEE* and Hussam Amrouch, *Member, IEEE*

Abstract—Brain-inspired hyperdimensional computing (HDC) is continuously gaining remarkable attention. It is a promising alternative to traditional machine-learning approaches due to its ability to learn from little data, lightweight implementation, and resiliency against errors. However, HDC is overwhelmingly data-centric similar to traditional machine-learning algorithms. In-memory computing is rapidly emerging to overcome the von Neumann bottleneck by eliminating data movements between compute and storage units. In this work, we investigate and model the impact of imprecise in-memory computing hardware, namely TCAM cells, on the inference accuracy of HDC. Our modeling is based on 14 nm FinFET technology fully calibrated with Intel measurement data. We accurately model, for the first time, the voltage-dependent error probability in SRAM-based and FeFET-based in-memory computing. Thanks to HDC's resiliency against errors, the complexity of the underlying hardware can be reduced, providing large energy savings of up to 6x. Experimental results for SRAM reveal that variability-induced errors have a probability of up to 39 %. Despite such a high error probability, the inference accuracy is only marginally impacted. This opens doors to explore new tradeoffs. We also demonstrate that the resiliency against errors is application-dependent. In addition, we investigate the robustness of HDC against errors when the underlying in-memory hardware is realized using emerging non-volatile FeFET devices instead of mature CMOS-based SRAMs. We demonstrate that inference accuracy does remain high despite the larger error probability, while large area and power savings can be obtained. *All in all, HW/SW co-design is the key for efficient yet reliable in-memory hyperdimensional computing for both conventional CMOS technology and upcoming emerging technologies.*

Index Terms—Reliability, In-memory Computing, Hyperdimensional Computing.

1 INTRODUCTION

In recent years, machine-learning models based on traditional algorithms like Deep Neural Networks (DNNs) have made steady progress. Such advancements are often associated with larger, more complex neural networks, further increasing their already large demand for processing power and memory. The traditional von Neumann architecture is reaching its limits for such overwhelming data-centric applications. As a matter of fact, data movement between memory and compute units profoundly contributes to the total energy consumption [1] and does form the key bottleneck. Furthermore, the significant amount of training data and the iterative training concept to tune the model's weights both exacerbate the energy and processing-power challenges. Dedicated hardware accelerators, like Google's Tensor Processing Units (TPUs), aim at accelerating NN inference and training with large power-hungry on-chip memories. In such accelerators, the data is moved from external memory to the on-chip memories once and then repeatedly feed to the systolic MAC arrays reducing off-chip data movement. Emerging non-volatile memories consume less energy but are not as reliable as conventional CMOS-based SRAMs. However, DNNs are very susceptible to bit

errors in which a single bit flip can drop the inference accuracy to almost zero [2].

Brain-inspired Hyperdimensional Computing (HDC) addresses the challenges of costly iterative training and the need for large amounts of training data. Similar to the human brain, patterns can be learned in one iteration from little training data. For seizure detection, a few samples are sufficient [3]. To create such an HDC model, only a single pass over the data is sufficient. This capability is called *one-shot learning* and avoids the costly iterative training required by DNNs. In addition, HDC operations, unlike in DNNs, do not rely on expensive floating-point matrix multiplications during training but are lightweight and highly-parallelizable bitwise operations. The same operations are furthermore used for both training and inference, avoiding two distinct hardware implementations. All of this is achieved through the use of vectors with thousands of independent components – *hypervectors*. Hence, an individual component has little impact on the overall accuracy resulting in high robustness against noise in the underlying memory as well as a high resiliency against errors in the performed operations [4]–[6]. HDC has been successfully applied to a wide range of application domains such as language recognition [7], gesture recognition [4], seizure detection [3], image classification [5], and more. In all applications, the inference operation associates an unlabeled query hypervector with the previously-trained class hypervectors by computing a similarity metric between them (e.g., Hamming distance). The computation is done in the Associative Memory (AM), which stores the class hypervectors. With traditional computer architectures, the processing unit has to compute the similarity with

• Simon Thomann, Paul R. Gessler, and Hussam Amrouch are with the Chair of Semiconductor Test and Reliability (STAR), University of Stuttgart, Stuttgart 70569, Germany. E-mail: {thomansn, gessler, amrouch}@iti.uni-stuttgart.de. Simon Thomann and Paul R. Gessler have contributed equally.

The developed framework and models are publicly available at <https://opensource.milcad.org>.

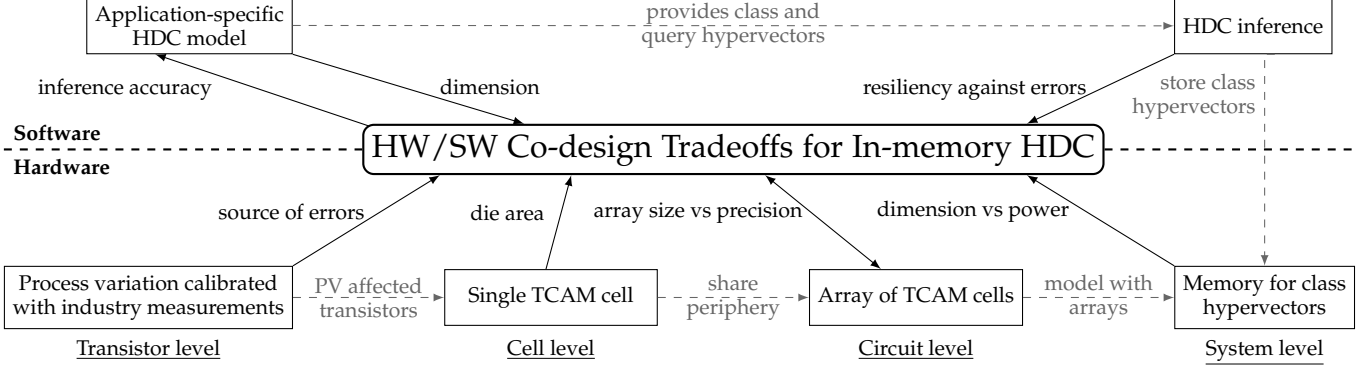


Fig. 1. Overview of our cross-layer (from transistor to software application) framework for in-memory hyperdimensional computing. It enables the investigation of several tradeoffs at both hardware and software level.

each class. Because of the hypervectors large size (e.g., 10 kbits), data movement is again a bottleneck in existing von Neumann architectures when employed to implement HDC, especially in regards to applications with a large number of classes.

Novel In-memory Computing architectures address this bottleneck by implementing the similarity computation directly within the memory where the data resides. The class hypervectors are not stored in regular memory but in a Ternary Content Addressable Memory (TCAM) [8]. In the traditional address-based memory concept, an address is provided to retrieve data. In a TCAM, the data is provided, and then its address is returned if the data exists. This approach can also be used for inference in HDC. If the unknown query hypervector is applied as “data” to the TCAM, the result is not the address but the similarities to each class. Therefore, the inference can be fully parallelized, accelerating this step. In addition, applying the query hypervector is the only data movement reducing the energy costs significantly. However, the in-memory operations are less precise due to their analog implementation. The quality of the peripheral circuitry and device-to-device process variation seriously impact the precision, especially in nano-scaled devices (e.g., 14 nm nodes and below). This holds even more when it comes to emerging memory technologies. Emerging non-volatile memories (NVMs), like Spin-Transfer Torque Magnetic RAM (STT-MRAM) [9], Resistive RAM (ReRAM) [10] or Ferroelectric FET (FeFET) [11], promise an increased energy and area efficiency over conventional SRAM technology. Their single-device design require less die area compared to traditional 6T or 8T SRAM cells [12]. Furthermore, emerging NVMs consume significantly less power since they are non-volatile and can be turned off without loss of data [12]. However, these technologies are not yet as mature as CMOS-based SRAM and are therefore more affected by variation [13]–[15]. Nevertheless, HDC is inherently resilient against errors. Hence, the software can tolerate imperfect yet more efficient hardware, and HW/SW co-design becomes essential.

Our key focus in this paper is in-memory brain-inspired hyperdimensional computing. Based on 14 nm FinFET model fully calibrated with Intel measurements for both transistor characteristics and variability, we implement an SRAM-based TCAM to compute the similarity metric Hamming distance directly within the memory. The hypervector is divided into blocks and mapped to individual TCAM

arrays. The computation is less precise in larger blocks and is additionally impacted by process variation. Thus, we model the probability of error in the Hamming distance computation based on block size and operating voltage in order to explore the available design space and the existing tradeoffs. Independent of the hardware, at the software level, we model the impact of imprecise distance computations on the inference accuracy for different block sizes. Finally, we combine both models into a framework to investigate the reliability of in-memory hyperdimensional computing. Based on this, we explore various HW/SW co-design tradeoffs.

Figure 1 provides a general overview of our work starting from the transistor level to circuit level all the way up to the software level and the final HW/SW co-design. With a given set of application-depended class and query hypervectors, our flow enables the exploration of various tradeoffs. We explore two different applications (language classification and image classification), showing how software matters and HW/SW co-design is key. As shown, our framework has well-defined interfaces to accommodate different circuit-level models for the similarity metric computation. Therefore, our work is not limited to a certain technology node. Other technologies can be integrated within our framework as long as they offer energy, computation latency, and error probability models. In this work, we investigate not only conventional CMOS-based SRAM, but also emerging NVM-based Ferroelectric FinFET (Fe-FinFET). The latter promises a higher area and energy efficiency at the cost of a higher probability of error. To ensure fair comparisons, our Fe-FinFET device model is based on the same 14 nm FinFET baseline and is subject to the same amount of variations.

Existing works lack several key aspects. In [16], a large monolithic array of 45 nm SRAM-based XOR gates and counters has been proposed, whereas we utilize advanced 14 nm FinFET TCAMs. In combination with the fact that process variation was not considered in [16]; hence, no errors could be modeled. We employ a calibrated transistor characteristics and variability model that allows us to correctly investigate the impact of process variation on the inference accuracy. In a proposed ReRAM-based crossbar, the process variation model is basic, and its impact is hidden by slower computation [16]. We demonstrate that in SRAM-based designs, process variation cannot be addressed similarly and instead requires a higher voltage increasing energy consumption. The tradeoff between energy and inference

accuracy in [16] is based on a simplified assumption about the impact of errors in HDC. We show that the resiliency against errors of HDC is much larger. A FeFET-based TCAM design was proposed in [17]. They consider process variation but only for the older MOSFET design, whereas FinFET is much more susceptible to variation. In contrast to our work they do not evaluate the impact on the inference accuracy at software level.

Distinction from existing work: None of the existing works consider detailed cross-layer modeling starting from the transistor level all the way up to the software level in a holistic way. We demonstrate that HW/SW co-design is the key to efficient yet reliable in-memory HDC computing.

Our novel contributions within this paper are as follows:
(1) At the software level, we investigate how imprecise similarity metrics computations impact the inference accuracy of different HDC models. We divide the hypervectors into small blocks and limit the largest detectable Hamming distance.
(2) At the hardware level, we model the energy consumption as well as the probability of errors in the underlying SRAM-based TCAM caused by block size, process variation, and voltage. For accurate modeling, we employ 14 nm FinFET technology fully calibrated with Intel measurement data. Further, we extend our model to additionally account for the Fe-FinFET technology. This allows, for the first time, a fair comparisons of the reliability of in-memory brain-inspired HDC when implemented with conventional SRAMs vs. emerging NVMs
(3) Based on (1) and (2), our HW/SW co-design explores the impact of error-prone TCAM-based similarity computations on the inference accuracy for the first time. It reveals that HW/SW co-design opens doors to eliminate hardware errors and keep variability effects, which are very challenging in nano-scaled technologies, at bay. We further explore the tradeoff between energy and inference accuracy under process variation, demonstrating energy savings of 6x through voltage reduction is possible despite the high induced probability of error of up to 39 %. We demonstrate that Fe-FinFET has higher losses in the inference accuracy and propose a replica technique to mitigate those losses to the level of SRAM.

2 HYPERDIMENSIONAL COMPUTING

HDC has been recently researched in a wide range of application domains [3]–[5], [7]. The concept itself was proposed by Kanerva in 2009 [7]. The technique can detect patterns and classify data by mapping real-world entities into HD space. Such a space is created by hypervectors with hundreds or thousands of components, including simple bits, integers, real or complex numbers. While each type of hypervector has its own implementations of four basic operations, the semantics remain the same. To map complex real-world entities into the HD space, first, some hypervectors are created randomly to represent basic real-world values. The individual components of the hypervector are independent. Hence, an error in one place barely changes the represented real-world value. In contrast, numbers in traditional binary representation change drastically if a single significant bit is flip. Thus, HDC is intrinsically robust against noise and

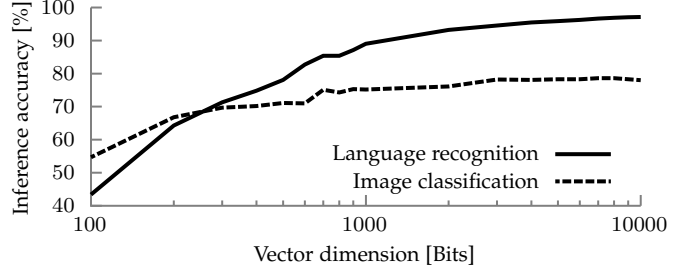


Fig. 2. The inference accuracy depends on the dimension of the hypervectors and targeted classification problem.

resilient to faults [4]–[6], [18]. Due to the very high dimensionality, the likelihood that two hypervectors are *orthogonal* is very large. Two binary hypervectors are orthogonal if their normalized Hamming distance is approximately 0.5. This metric is determined by the number of individual bit pairs that are different between both hypervectors. In other words, the number of ones in their XOR product. The resulting number is divided by the length of the hypervectors to normalize it. For other types of hypervectors, the operation (*measure similarity*) is determined differently but retains its meaning.

Using the generated hypervectors, the complex real-world entity can be encoded into HD space with the other three basic operations: addition \oplus , multiplication \circledast , and permutation Π . The addition \oplus bundles two or more hypervectors into a single hypervector of the same dimension. The multiplication \circledast binds two or more hypervectors together. The third operation, permutation Π , operates on a single hypervector and makes it orthogonal to itself.

2.1 Language Recognition with HDC

To detect the language of an unknown text, not only are the letters' frequencies important but also typical combinations of them, like “-ing” or “-tion” in English. The n -gram data structure is able to capture both aspects by encoding n individual letters L_i and their relation to each other through permutation [19]. The letter hypervectors HV_A to HV_Z are created randomly once, remain unchanged, and are stored in the Item Memory (IM).

$$HV_{n\text{-gram}} = HV_{L0} \circledast \Pi^1(HV_{L1}) \circledast \dots \circledast \Pi^{n-1}(HV_{Ln-1})$$

With a sliding window of size n , the whole text is encoded and the n -grams are added together to form a single hypervector. To train the HD model, for each language (class) a reference text is encoded. The class hypervector to language mappings are stored in the AM, the HD model. During inference, the unknown text is encoded with the same n -gram technique and the same hypervectors from the IM. The encoded hypervector is presented to the AM as a query. The similarities to all stored class hypervectors are computed. The label (i.e., language) of the class hypervector with the highest similarity is returned as the classification result.

In this work, we focus on binary hypervectors. The n -gram encoding is done with $n = 4$ as it yields the highest inference accuracy [19]. Eight different European languages are each trained with 1 million characters from the Wortschatz Corpora [20]. For inference, a query for each language

is created with 1000 sentences from the Europarl Parallel Corpus [21]. The dependency of the inference accuracy on dimension is shown in Figure 2. Increasing the dimension beyond 10,000 would benefit the accuracy only marginally. Hence, we limit the investigation to 10,000-bit hypervectors.

2.2 Image Classification with HDC

HDC has been explored for simple image datasets like MNIST [22], Fashion MNIST [23], or character recognition [5]. Those datasets have very homogeneous samples without rotations or translations. Hence, the HDC encoding does not need to capture such transformations. If, for example, images were rotated by 90°, the HDC model has to be retrained to recognize those rotated images. Another approach was proposed in [24], where multiple class hypervectors are trained and stored to represent a single class (i.e., they have the same label). For more complex datasets like Omniglot, [25], [26] employed a CNN as a feature extractor and HDC as a classifier. This approach was extended in [18] for CIFAR-100 and miniImageNet. However, without such preprocessing, image classification with HDC alone remains a challenge.

The MNIST dataset is a common benchmark and does not mandate any processing. It includes a total of 70,000 labeled images [27] for the ten digits from zero to nine. The images have a uniform size of 28×28 pixels. For each of the 784 pixel positions, a random hypervector is generated. The gray-scale images are binarized, and the position hypervectors of all white pixels are bundled into a single image hypervector. Per class, 6000 image hypervectors are selected for training and bundled into a class hypervector. No further processing, like retraining, is done. The AM contains ten classes (digit 0 to 9) and is queried with the remaining 10,000 image hypervectors.

2.3 TCAM Implementations for HDC

Various TCAM implementations for HDC have been proposed. They improve on TCAM’s inherently low precision argued for in [25]. In [26], a 3-bit FeFET multi-bit CAM (MCAM) achieves a similar inference to the PCM-based implementation proposed in [25]. Both approaches employ a CNN in the first stage and report results for the Omniglot image dataset.

In [28], a multi-bit HDC design (hypervectors with few-bit components instead of 1-bit binary) based on multi-level cell (MLC) FeFET is proposed. The k class hypervectors are stored in a $k \times 64$ crossbar of MCAM cells originally proposed in [26]. With MCAMs, the distance metric is not the Hamming distance or cosine similarity, but a semi-linear relationship between the distance and the conductance of the MCAM cell. The HDC model is retrained to work with the new distance metric. The impact of process variation is not evaluated. Only random bitflips during the encoding and the inference operation are injected, which does not accurately model the variation described in [26]. In our work, we model process variation accurately in the TCAM cells and thus can investigate its impact on the inference accuracy.

In [24], a pure binary HDC training and inference was described. They use a crossbar of ReRAM-based CAM cells to store the class hypervectors. Each row, which stores a complete hypervector, is connected to a shared wire. Before an inference operation, this wire is precharged. When the

query hypervector is applied, CAM cells with mismatching bits form a conducting path and discharge the shared wire. The row with the least mismatches (i.e., the most similar hypervector) discharges the slowest. A special CAM sense amplifier detects which of the shared wires discharges the slowest and finishes last. The hypervector stored in the row with this slowest discharge is the inference result. Process variation is considered in their SPICE simulations but only translated to a constant Hamming distance error. They do not report any incorrect computations because of it. However, process variation has a higher impact at smaller process nodes, like 14 nm employed in this work compared to 45 nm in [24].

3 HARDWARE-LEVEL ANALYSIS AND MODELING

In typical memory, an address is provided to return data. In Content Addressable Memory (CAM), data is provided and, if the data is already present in the memory, its address is returned. A TCAM is an extension and allows a lookup with “don’t care”. This lookup capability makes TCAMs perform best in search operations. While in typical memory, the data at each address would have to be compared sequentially, in a TCAM the lookup is parallelized. Hence, latencies within a few clock cycles can be achieved. TCAMs are therefore already used in ultra-high performance applications like network switching [29] or search engine accelerators in databases [30]. The third “don’t care” state can be used, for instance, to perform masked IP address lookups [31]. In HDC, the AM can be implemented efficiently with a TCAM avoiding costly data movement. The query hypervector represents the data to search for. Instead of address lockup, the Hamming distance to all stored class hypervectors can be computed in parallel. Therefore, instead of “search” it is called “comparison” in the rest of the paper.

In this section, we first introduce our calibrated CMOS transistor model that includes process variation. Second, we describe the SRAM-based TCAM cell design and, based on it, the block structure to store and compare a part of a hypervector. Then we use the process variation data from our transistor model to derive the error probabilities for each Hamming distance depending on voltage and block size.

3.1 Technology Modeling: 14 nm FinFET Calibration

In this work, we reproduce Intel’s 14 nm FinFET measurements [32] for their mature high-volume manufacturing process. With SPICE simulations, we carefully tune the transistor model-card parameters for the the industry-standard compact model of FinFET (BSIM-CMG [33]) until they are in excellent agreement with the measurements, both for nFinFET and pFinFET, as demonstrated in Figures 3(a) and 3(b). This applies to both, the I_D - V_G and I_D - V_D transistor properties. In a second step, we calibrate the model against the measurements for device-to-device variability. All important sources of manufacturing variability (gate work function, channel length, fin height, fin thickness, and effective oxide thickness) are modeled for a comprehensive representation of the process variation. Based on the calibrated compact industrial model presented first and Monte-Carlo SPICE simulations, we calibrate the standard deviations for each

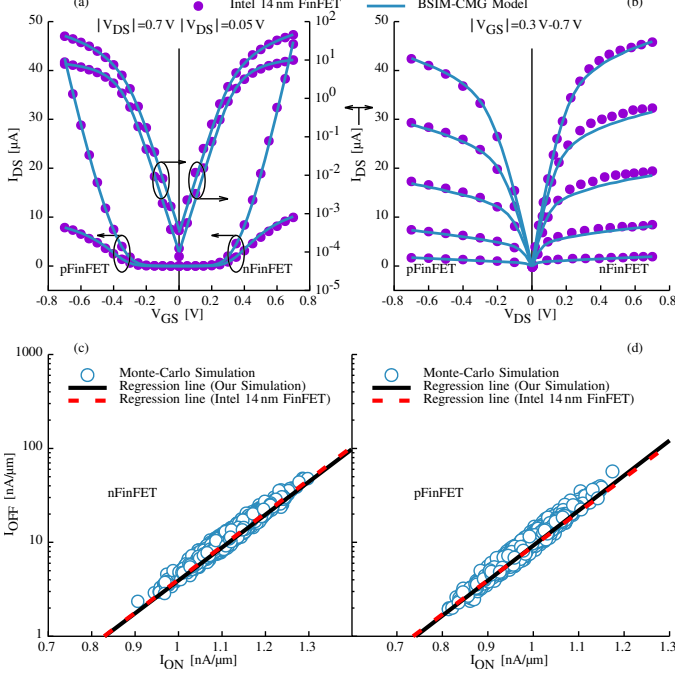


Fig. 3. Transistor calibration and validation against Intel 14 nm FinFET measurements extracted from [32]. The industry compact model of FinFET technology (BSIM-CMG) is calibrated to match Intel data for both nMOS and pMOS transistors for all different biasing conditions (a and b). The impact of process variation is also validated against Intel 14 nm FinFET for both nMOS and pMOS transistors in (c) and (d), respectively.

mentioned source of variability. Figures 3(c) and 3(d) demonstrates that variation in the I_{ON} vs. I_{OFF} from our Monte-Carlo SPICE simulations are in excellent agreement with the measurements from Intel.

3.2 Single TCAM Cell

A single TCAM cell with a 16 CMOS-transistor design couples two SRAMs S1 and S2 as shown in Figure 4(a) [17]. The cell's data C , a single bit of a class hypervector, is written to the two SRAMs in a complementary fashion. For instance, when $C = 1$, S1 and S2 are in the logical 1 and 0 state. A single SRAM is a bi-stable element formed by an inverter loop, the labeled nodes ('L' and 'R') are on the negated side. The left SRAM S1 holds 1, but its negated 'L' node expresses the inverted value 0. For a lookup, the Match Line (ML) is pre-charged. Then the query data Q is applied to the Select Line (SL) (corresponds to the left SRAM S1) and inverted to SLB (corresponds to the right SRAM S2). If it is a *match* ($C = Q$), then the inverted 'L' and SL are complementary ($\bar{C} \neq Q$) and no conductive path from GND to the ML is formed. The TCAM cell is OFF because the voltage stays high. The same logic applies analogously to the right-hand side for the non-inverted 'R' and inverted SLB ($C \neq \bar{Q}$). If it is a *miss*, either 'L' and SL or 'R' and SLB are active at the same time, their associated transistors form a conductive path and discharge the ML. The TCAM cell is ON.

3.3 Our SRAM-based TCAM Array

Each individual TCAM cell stores a single bit of a class hypervector. Multiple cells are combined into a *block* to

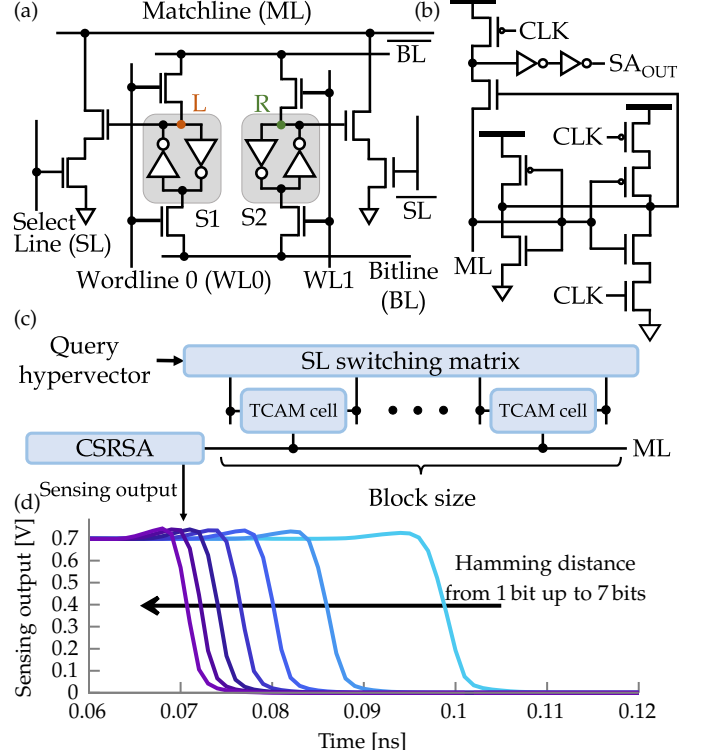


Fig. 4. (a) Schematic of a standard 16T TCAM cell. (b) The schematic of the clocked self-referenced sense amplifier (CSRSA). The CLK is the enable signal. (c) Full TCAM array circuit. The number of cells (block size) is variable. Only the select line (SL, input) and match line (ML, output) are drawn. (d) Example of the output voltage waveforms of the CSRSA for a block size of 15 bits.

represent multiple bits of a partial hypervector. All TCAM cells in the block share the same periphery and access logic as shown in Figure 4(c). This includes the Bit Line (BL) and Word Line (WL) to write the class hypervector. In our model, this write operation occurs only during an initialization phase and thus is not within the focus of our framework. Hence, we exclude it from the evaluation and also simplify the SPICE circuit implementation by replacing the BL and WL with individual voltage sources.

The ML is shared with all TCAM cells within one block and an integral part of the TCAM block design. Before an inference operation, the ML is pre-charged. Then the respective bits of the query hypervector are applied to the block. Recall that each block only represents a few bits of the class hypervector, and thus only the respective bits of the query hypervector are applied. In each individual TCAM cell, the applied bit and the stored bit are compared as described in Section 3.2. If the result is a miss, the TCAM cell will establish a conductive path from the ML to GND and discharge the ML. The more misses occur, the more conductive paths are established, the faster the ML discharges due to the smaller total resistance. In other words, the discharge rate reflects the number of cells reporting a miss. The number of misses between the stored partial class hypervector and the applied partial query hypervector is equal to the partial Hamming distance. Hence, in practice, a TCAM block realizes the Hamming distance computation.

In our SPICE simulations, the ML is connected to a clocked self-referenced sense amplifier (CSRSA) [17]. Its

schematic is illustrated in Figure 4(b). The CSRSA converts the discharge rate from the voltage domain (how fast is the ML discharged) to the temporal domain (when does the voltage drop). This operation latency determines the partial Hamming distance of this block. An example is shown in Figure 4(d) for a block size of 15 and Hamming distances from one to seven bits. Similar to [16], we observe a linear dependency between the number of misses and the discharge rate. While one and two misses are clearly separated by 0.01 ns, this gap roughly halves between two and three misses. The size of the gaps also depends on the size of the block, since large blocks have higher parasitic capacities increasing the discharge time for any number of misses. Nevertheless, separating large Hamming distances is challenging and impacted by block size and voltage. Determining the largest detectable distance and attributing a cost in terms of chip area, additional operation latency, or energy is implementation-specific. Models can be provided for our framework to include such costs into the analysis, extending the explored space.

In this work, we consider TCAM blocks from a size from two bit up to 25 bits. At this upper limit, our evaluation points to a low inference accuracy in conjunction with the maximum precision of 7 bits. Hence, any larger block sizes would result in low-accuracy systems. For a full AM (e.g. 10,000 bits), multiple block instances are required to store a full hypervector.

3.3.1 TCAM Block Energy Consumption

The block size affects energy consumption. Larger blocks naturally require more energy but their TCAM cells all share the same periphery; in our circuit, the CSRSA. Hence, their overhead per bit is smaller. The energy consumption of a single block is accurately extracted from the SPICE simulations. All currents over the operation latency of the complete similarity computation are integrated. The operation latency is the time between the flank of the CSRSA's enable signal and the output voltage dropping below 50% V_{DD} . It is noteworthy that our framework is modular, and hence any other alternative latency and/or energy models can be included. In the targeted 14 nm FinFET technology, the nominal voltage is 0.7 V. To explore existing tradeoffs between reliability, operation latency, and energy under the effect of voltage, we study a wide range of operating voltages starting from 0.5 V up to 1.0 V.

3.4 Modeling the Error Probability

In this work, the Hamming distance is derived from the operation latency of a block (TCAM cells and CSRSA). The shorter the latency, the higher the Hamming distance. However, the operation latency varies from block to block as shown in Figure 5. This variation in latency stems from the variation in the underlying transistors. Such variation is inherent to every manufacturing process. It impacts key electrical characteristics of each transistor and hence the reliability and speed of a TCAM cell. In other words, some cells establish a stronger conductive path from the ML to GND, some cells a weaker path. The consequences of these different discharge times of the ML are the different operation latencies. Hence, the underlying variation directly impacts the Hamming distance computation and can cause errors.

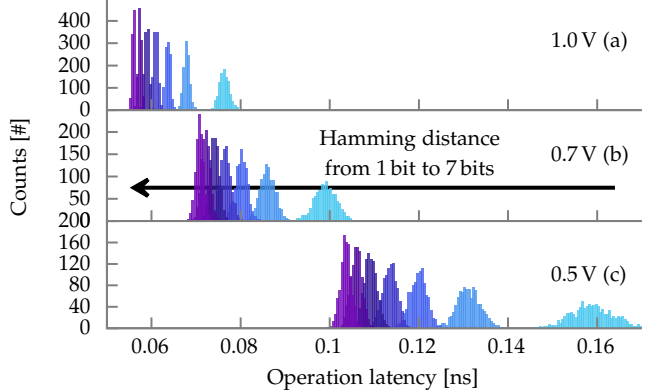


Fig. 5. The operation latencies under process variation at three different supply voltages (a, b, and c). The block size is 15 bits. The results are based on 1000 Monte-Carlo SPICE simulations per voltage level and Hamming distance.

Our calibrated process variation model (see Figures 3(c) and 3(d)), described in Section 3.1, is applied to the underlying transistors of a TCAM cell. We conduct 1000 Monte-Carlo SPICE simulations per block size and all possible Hamming distances. The variation-free nominal operation latencies are shown in Figure 4(d), whereas the results of the Monte-Carlo SPICE simulations are presented as histograms in Figure 5 for three different voltages. We analytically model the operation latency distribution for each Hamming distance and build our probabilistic error model. Without process variation, our framework then maps the nominal operation latency to a Hamming distance (Figure 4(d)). With process variation, the framework samples the operation latency distribution (Figure 5) of the nominal Hamming distance. If the variation from the nominal operation latency is larger than half the distance to the neighboring Hamming distance, then this neighboring Hamming distance is reported as the result of the computation. Since this is the incorrect distance, it is counted as an error. As it can be seen from Figure 5, most incorrect Hamming distances are within one bit of the nominal distance. Only for large distances (i.e., small latencies), higher deviations are possible. The error probabilities for the block size of 15 bits are shown in Figure 6. The maximum detectable Hamming distance is defined as seven bits; any shorter operation latency is also reported as seven bits. While three bits, due to variation, can be incorrectly reported as two or four bits, seven bits cannot be reported as eight bits because of the definition of a maximum detectable Hamming distance. Thus, the error probability for seven bits is lower.

3.5 Impact of Operating Voltage

A higher supply voltage V_{DD} increases the gate voltage at the two transistors on the discharge path. Thus, the discharge rate is higher and the increase of I_{ON} dominates the linear increase of charge Q of the ML. The increase of V_{DD} also reduces the spread of the individual Hamming distance groups. As shown in Figure 6, this directly influences the error probability. Contrary to the expectations, 0.5 V performs better than 0.7 V. A detailed analysis with finer voltage steps reveals that the interaction between operation latency and spread of the distributions benefits 0.5 V. The lower

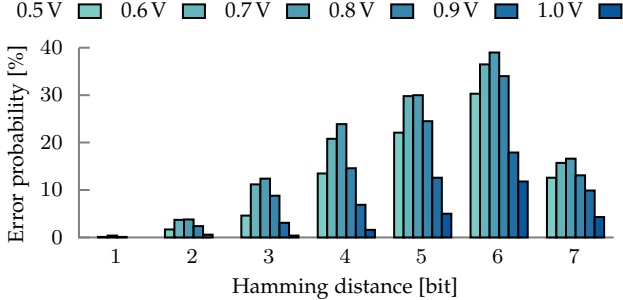


Fig. 6. Error probabilities of the individual Hamming distances under process variation at different supply voltages V_{DD} . The error probability is lower for the highest Hamming distance as there is no overlap with an even higher Hamming distances. The unintuitive observation of 0.7 V having the highest error probability is explained in Section 3.5. The block size is 15 bits and the maximum detectable Hamming distance is seven bits. The results are based on 1000 Monte-Carlo SPICE simulations per voltage level and Hamming distance.

voltage causes wider distributions but those are farther apart. With 0.7 V, the distributions are narrower but closer together, resulting in higher overlap and a higher probability of error. The drawback of the high 1.0 V level is higher energy consumption. Even though the discharge rate is higher, the number of charge carriers that have to be moved increases as well. This increase is directly proportional to the energy and outweighs other reductions.

However, HDC's resiliency against errors creates the opportunity for energy savings. If a higher error probability can be tolerated by the HDC model, than a voltage reduction also reduces the energy consumption. At 0.5 V, a 15-bit block consumes 0.73 fJ per similarity computation in contrast to 4.53 fJ at 1.0 V. The numbers are derived from our SPICE simulations as discussed in Section 3.3.1. With our HW/SW co-design framework, the tradeoff between inference accuracy and energy consumption is investigated in Section 5.

4 SOFTWARE-LEVEL ANALYSIS AND MODELING

At the software level, the inference accuracy for an HDC model is determined. Our framework only requires the encoded class and query hypervectors. Therefore, it is agnostic to the actual application and the encoding of the hypervectors. Currently, only binary hypervectors are investigated since the underlying hardware models only supports Hamming distance computation.

In-memory Hamming distance computation based on TCAMs/CAMs is restricted to a maximum vector length as shown by our TCAM block design in Figure 4 and others [16], [17]. Such a block could be, for example, a TCAM array or an ReRAM crossbar [16]. In case of TCAM cell designs, the higher Hamming distances overlap significantly, making their separation difficult as shown in Figure 5. Note that the figure does not include the latencies for the Hamming distances from 8 bits to 15 bits because their overlap makes them indistinguishable in practice. In the proposed design, the time-to-digital converter (TDC) is responsible to differentiate the latencies. Its temporal resolution correlates with its implementation complexity. In other words, a high-resolution TDC could differentiate the mean latencies of high Hamming distances. However, because of the underlying

variation, the latencies of high Hamming distances overlap significantly leading to incorrect results in most cases. A high temporal resolution has diminishing returns but an increasing implementation complexity. To avoid this needless complexity of the TDC, the detectable Hamming distance is limited by the designer. This limit is referred to as *precision* in this work. It is a simplification that aims to reduce the implementation effort of a block by limiting the reported Hamming distance. As an example, the 15-bit block in Figure 4(d) only reports correctly until seven bits; any higher difference is also reported as seven. The TDC is emulated by our framework and not part of the SPICE simulations.

Our software-level analysis is orthogonal to the underlying hardware and relies on models. Initially, a model of error-free and variation-free hardware is assumed. It accepts a partial class and query hypervector and always computes the correct Hamming distance. This computation is repeated for all parts of the class and query hypervector and all classes. The class with the lowest Hamming distance is selected as the inference result. The result is compared with the true label associated with the test hypervector. If the inferred class and the true label match, then the inference is correct. The overall inference accuracy is the ratio of correctly classified test samples to the total number of test samples. Based on the assumption of an ideal hardware implementation of a block, the inference accuracy is as high as possible for the given HDC model.

In Figure 7, different block sizes and precision are shown with the examples of language recognition and image classification. As a general observation, the inference accuracy starts to drop significantly if the precision of a block is limited to less than half of its size. This is to be expected since information is lost for larger Hamming distance. A small distance in another block cannot compensate for that. Interestingly, in the image classification application, the inference accuracy does not drop as fast. The reason is the already high overlap of the class hypervector with each other. On average, their normalized Hamming distance is 0.21 in contrast to 0.44 for languages as shown in Table 1. In other words, the diversity in the image classification model is lower. Consequently, most queries are similar to the class hypervector and have a lower Hamming distance. Precision does not limit as much. This suggests the possibility of a precision-aware encoding scheme to increase the similarities of the classes while at the same time retaining high inference accuracy.

Another approach is the generation of quasi-orthogonal hypervectors through metalearning with a CNN as a trainable encoder [25]. In [25], 13,180 floating-point hypervector of dimension 512 from 659 classes were created. To align with the previously evaluated classification benchmarks, all hypervectors belonging to a common class are averaged to create a class hypervector. In addition, all hypervectors are binarized with a simple threshold. Their average Hamming distance is 0.49, higher than for the language dataset (0.44) demonstrating the CNNs ability to maximize the distance.

The baseline inference accuracy with floating-point hypervectors and cosine similarity is 94.3 %. After binarization and with Hamming distance, the inference accuracy becomes 93.4 %. The results for SRAM-based TCAM are summarized in Table 1 and use those binary hypervectors as a baseline. As expected, without process variation and full precision

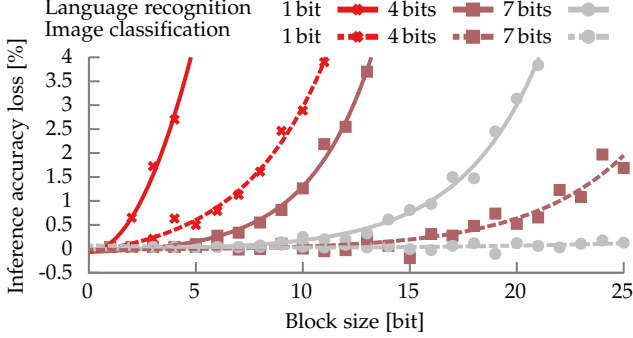


Fig. 7. Loss in inference accuracy due to different precision levels (in bits). Image classification (dashed lines) is more resilient to imprecision than language recognition (solid lines). Lines are fitted to data (symbols).

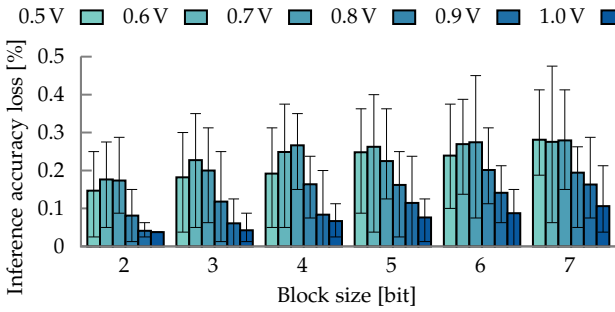


Fig. 8. Loss in inference accuracy due to process variation for language recognition using 10,000 bit.

(block size $N=7$, precision $P=7$), no loss in inference accuracy is reported. A reduced precision ($N=15$, $P=7$) only impacts the language recognition dataset, Omniglot or MNIST are not affected. This shows that there is no strong dependency between the average Hamming distance of the class hypervectors and an accuracy loss due to a reduced precision. A limited precision, e.g., to half of the block size, limits the detectable Hamming distance to 0.5 (normalized). This matches the intended distance to all but the correct class with the quasi-orthogonal prototypes. The Hamming distance to the correct class is lower and thus less impacted by a reduced precision.

Because of process variation, even a full precision design reduces the inference accuracy by up to 0.28 %. The MNIST dataset is again less impacted because a vector size of 10,000 used in this experiment includes ample redundancy. In contrast to a design free of process variation, a reduced precision impacts all datasets.

5 HW/SW CO-DESIGN AND EVALUATION

For a holistic analysis of an in-memory HDC system, models at hardware and software level have to be integrated. In this section, we demonstrate the promise of HW/SW co-design to obtain an efficient design solution. The error properties of the underlying hardware are jointly considered with the error resiliency of the target application at the software level.

5.1 Experimental Setup

At the transistor level, we employ our 14 nm FinFET model described in Section 3.1. The TCAM cell design and the

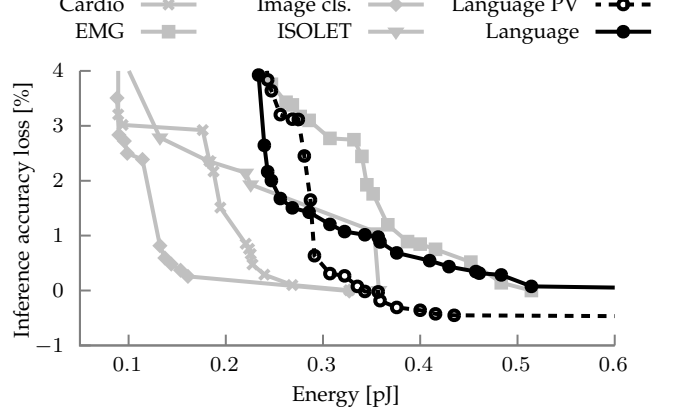


Fig. 9. Pareto fronts for different hardware configurations. A precision level of 7 bits is considered. Impact of Process Variation (PV) is, additionally, demonstrated for “language recognition”.

TCAM block circuit is described in Section 3.2 and Section 3.3, respectively. The error model is developed in Section 3.4. We evaluate the inference accuracy with five applications in total. Language recognition and image classification are introduced in Section 2. To confirm our analysis and conclusion, we additionally evaluate EMG gesture detection [34], voice recognition ISOLET [35], and heart disease detection CARDIO [35]. The design space includes the voltage levels 0.5 V, 0.7 V, 0.8 V, and 1.0 V, block sizes from two to 25 bits, and an application-dependent subset of dimensions from 2000 bits to 10,000 bits. The hypervectors are partitioned and assigned to the TCAM blocks. The similarity metrics are computed per block and provided to the error model to capture the impact of process variation. Additionally, the energy consumption of each TCAM block, which depends on the Hamming distance, is aggregated. The inference accuracy and energy consumption form one point in the design space. Any form of preprocessing, such as encoding of data samples, is not considered.

5.2 Impact of Variability-induced Errors

As discussed in Section 3.1, process variation is a major concern in advanced technologies such as FinFET. This is reflected in the probability of errors for a Hamming distance computation is close to 40 % at the nominal voltage of 0.7 V (Figure 6). However, the inference accuracy decreases at most by 0.45 % at 0.7 V (0.28 % on average) as shown in Figure 8. We have demonstrated in Figure 6 that a reduced voltage of 0.5 V actually reduces the probability of errors. This is reflected by an increased inference accuracy. To further lower the probability of errors, the voltage has been increased to 1.0 V resulting in a maximum loss of inference accuracy by 0.21 % (0.11 % on average), close to the fluctuations caused by the inherent randomness of any HDC model. These results show that HDC is also resilient against errors in the computation of the similarity metrics. Although the impact of process variation has to be considered, it does not dominate the tradeoffs available to a system designer.

5.3 Tradeoff Energy vs. Accuracy

Figure 9 shows the Pareto fronts in the design space for all five applications. The impact of the application on the

TABLE 1

Loss of inference accuracy with and without process variation (PV) and with full precision (block size $N = 7$, precision $P = 7$) and with reduced precision ($N = 15$, $P = 7$). The results show that the average Hamming distance between the class hypervectors does not correlate with a requirement for full precision.

Dataset	Avg. Hamming Distance	without PV		with PV	
		$N = 7, P = 7$	$N = 15, P = 7$	$N = 7, P = 7$	$N = 15, P = 7$
MNIST	0.21	0.00 %	0.00 %	0.05 %	0.11 %
Language	0.44	0.00 %	0.81 %	0.28 %	0.99 %
Omniglot	0.49	0.00 %	0.00 %	0.23 %	0.31 %

HW/SW co-design is discussed in the next section.

Voltage influences the impact of process variation on the inference accuracy as discussed in Section 5.2. Our HW/SW co-design shows that the increased energy consumption with 1.0V does not outweigh the accuracy gain for almost all configurations. A higher voltage is only Pareto-optimal if a permille in inference accuracy is required. However, due to the random nature of any HDC model, such small differences are overshadowed by a “lucky”, or “unlucky” initialization of the random item hypervectors. Hence, an increased voltage does not offer a significant benefit and instead offers the possibility to reduce energy consumption. Accordingly, the large majority of Pareto-optimal configurations use 0.5V.

Block size in relation to precision creates an upper bound on the inference accuracy for Pareto-optimal configurations. For example, to limit the accuracy loss to 2.5 %, the precision has to be at least half of the block size. A special case is a precision of one bit transforming the TCAM block into a comparator. Either all bits are equal (Hamming distance is zero) or all are different (Hamming distance is the block size). To maintain some accuracy, the only viable block size is two. With 10,000-bit hypervectors, the loss in inference accuracy is limited to 0.5 %. Indeed, for all Pareto-optimal configurations, losses smaller than 0.5 % require a high level of precision and small block sizes. In other words, full precision and little to no errors in the similarity metrics computation. However, process variation is still a source of errors, which have to be tolerated by the HDC model.

The **dimension** of the hypervectors creates a similar bound on the inference accuracy. The lowest energy consumption is achieved with 2000-bit hypervectors. For language recognition, about a quarter of the Pareto-optimal configurations use this dimension but do not exceed 96 % accuracy. A similar portion of the configurations use 9000-bit hypervectors and thus achieve the highest accuracy. This shows that the inherent resiliency against errors is not purely dependent on a higher dimension as a redundancy buffer.

5.4 Impact of Application on HW/SW Co-design

In Section 4, the similarities of the class hypervectors to each other are discussed for two applications. The ten class hypervectors of the image dataset are more similar to each other, whereas the class hypervectors in the language classification model are almost orthogonal. This difference impacts the resiliency against errors. The more similar class hypervectors in the image classification make the HDC model more resilient, as shown in Figure 7. The higher resiliency enables more potential for energy savings. Therefore, block sizes of up to 25 are Pareto-optimal for image classification. Additionally, the impact of process variation is

smaller compared to language recognition. The reason is the smaller Hamming distances of query and class hypervectors. As shown in Figure 6, the probability of errors is smaller for lower distances. Furthermore, the highest Pareto-optimal dimension is 8000 bits for images compared to 10,000 bits for languages. Pareto-optimal configurations for both applications only agree in 0.5 V and require different parameters otherwise. These differences highlight the importance of HW/SW co-design. If a 0.5 % loss in inference accuracy is acceptable, an efficient implementation of an image classifier saves $4.5 \times$ energy, whereas $11.5 \times$ is possible for languages.

5.5 Comparison to State of the Art

In [16], a 4-bit ReRAM crossbar is proposed for in-memory Hamming distance computation. Similar to our work with SRAM-based TCAM arrays, the hypervector is partitioned and mapped to the hardware blocks. In contrast to our approach in which HW/SW co-design is employed to eliminate variability-induced errors, they nullify the impact of process variation by increasing the operation latency. Therefore, errors only occur if they scale down the voltage of their circuit to reduce energy consumption. Due to the reduced voltage, the result of all Hamming distance computations is increased by one bit. For example, a distance of two bits is always reported as a distance of three bits. If the Hamming distance is four bits, five would have to be reported due to the shift. However, the 4-bit ReRAM crossbar can only report distances of up to four bits.

We implement their error model in our framework. Thanks to its modularity, we can quickly repeat the analysis analogously and evaluate their error model for different dimensions and applications. In their evaluation, the ReRAM crossbar array section that operates at a reduced voltage always causes an error of one bit in the Hamming distance. With the number of scaled voltage ReRAM crossbars (i.e., number of bit errors), they assigned an inference loss determined by a theoretical analysis of one application. In contrast, our framework evaluates the error models by executing the HDC models. We show that the ReRAM error model does perform better than previously reported. Their assumption, that each scaled voltage ReRAM crossbar causes one bit error, is too pessimistic because the shift applies to all crossbars and thus cancels out. Instead of 4.0 %, if all crossbars use a scaled voltage [16], the accuracy loss amounts to 0.2 %, which is comparable to the SRAM-based TCAM model for a dimension of 10,000 bits. The accuracy loss for other dimensions is comparable as well. For image classification, the impact of both error models on the inference accuracy is similar.

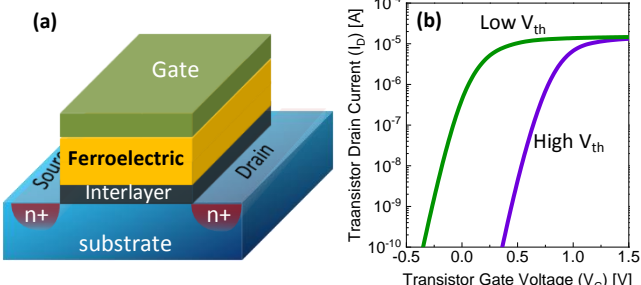


Fig. 10. (a) FeFET where the high- κ layer is replaced by a thick (8 nm to 10 nm) layer of ferroelectric material ($\text{Hf}_{0.5}\text{Zr}_{0.5}\text{O}_2$). (b) Polarizing the ferroelectric layer in the gate stack creates two distinguishable states, i.e., low V_{th} and high V_{th} , which correspond to high and low current, respectively.

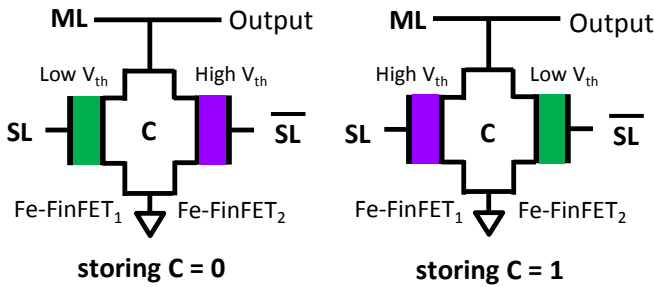


Fig. 11. Visualization of the complementary write scheme through low- V_{th} and high- V_{th} to store logic 0 and 1.

6 HDC WITH EMERGING NVM TECHNOLOGIES

Data-intensive workloads like big data and deep neural networks demand for larger on-chip memories. However, traditional CMOS-based SRAM consumes lots of power and chip area. With a slow-down in classical CMOS technology scaling, emerging NVM technologies gather more and more attention. Several different technologies have been proposed, e.g., STT-MRAM [9], ReRAM [10] or FeFET [11]. NVMs reduce the area demand since they do not require six or eight transistors like traditional SRAMs but only the memory device and typically one access transistor [36]. Furthermore, they retain their state while powered off, reducing static power consumption drastically. Thanks to these advantages over SRAMs, large on-chip memories are feasible. However, one major challenge faced by most NVMs is their compatibility with the CMOS fabrication process, preventing tight integration with logic transistors [37].

Hafnium Oxide (HfO_2) based FeFET addresses this challenge [11], [36]. FeFET devices, in fact, are regular CMOS transistors where a thick layer of ferroelectric (FE) material replaces the traditional high- κ layer as shown in Figure 10(a). Existing manufacturing processes can be employed for FeFET [38] since HfO_2 has been adopted as high- κ material since 2007 [39]. No additional process steps or new materials are required, only two additional masks [11], [40]. Thus, FeFET is the only fully CMOS-compatible emerging NVM [40], [41]. Additionally, the addition of the FE layer increases only the height of the transistor but not the footprint, enabling a high-density memory. The FE layer can be polarized with a write operation by applying a 4 V pulse. This creates two distinguishable states where the V_{th} of the FeFET is either

high or low as shown in Figure 10(b). The state is sensed by measuring the drain current at a given gate voltage.

Due to all of these advantages, FeFET has a high potential compared to other emerging NVMs to be commercialized into mainstream products in the near future. Therefore, FeFET attracts interest in academia and industry alike. GlobalFoundries has already demonstrated various prototypes [11], [40] and Intel has recently reported an endurance breakthrough of 10^{12} cycles [42]. Furthermore, only two FeFETs are necessary to implement a TCAM cell as shown in Figure 4(a) making a FeFET-based TCAM array 8 \times denser than an SRAM implementation [43] creating new tradeoffs.

6.1 Fe-FinFET-based TCAM Array

Previous works investigated planar MOSFET-based FeFETs, which are less susceptible to variation. In our implementation, we employ the Intel 14 nm FinFET model, also used in the SRAM-based design, as a base. To create a Fe-FinFET, the FE layer is added. Thus, the underlying FinFET base is complemented by a state-of-the-art ferroelectric physics-based compact model [17]. Since we employ the same calibrated model described in Section 3.1 for the underlying FinFET, we can study and compare the impact of process variation on Fe-FinFET and SRAM in a fair way for the first time. Our transistor level operation (initializing the polarization, write transistor into desired state) of the Fe-FinFETs is similar to recent state-of-the-art shown in [44]. To program the Fe-FinFETs, a 4 V pulse is applied for 10 μs to saturate the polarization for the best read performance. The state of the Fe-FinFETs changes rarely and only if the class hypervectors have to be updated. Hence, write latency and endurance are not of concern.

In contrast to the 16 CMOS transistor design, a Fe-FinFET-based TCAM only requires two Fe-FinFETs as depicted in Figure 11. Both designs use the complementary storing scheme described in Section 3.2. If a logical 0 has been stored in the TCAM, then Fe-FinFET₁ is in the low- V_{th} state (green). A logical 1 on the SL triggers the discharge and thus signals a miss. The structure of a full array is analogous to the design shown in Figure 4(c). Only the SRAM-based TCAM cells are replaced with Fe-FinFET-based TCAM cells.

6.2 HDC with Fe-FinFET Under Process Variation

To study an AM with a Fe-FinFET-based TCAM array, the methodology described in Section 3.3 is applied again. Comparability is ensured by applying the same capacity to the ML for both designs, Fe-FinFET and SRAM. The distributions of the operation latencies are shown in Figure 12. First, the voltage has a much higher effect on the latency compared to SRAM. Fe-FinFET is overall slower with up to 5.0 ns with one miss at 0.5 V. At 1.0 V, the latency is comparable to SRAM at 0.5 V. Second, the variation is higher, clearly visible by the large overlap of the latencies representing different Hamming distances. Similar to SRAM, higher voltages do reduce the overlap. At 0.5 V, the latencies for a one-bit Hamming distance spread from 0.8 ns to 5.0 ns. The sizeable overall overlap is due to Fe-FinFET's higher susceptibility to process variation compared to SRAM. This is expected since SRAM is a very mature technology in contrast to Fe-FinFET, which is still in the prototype stage.

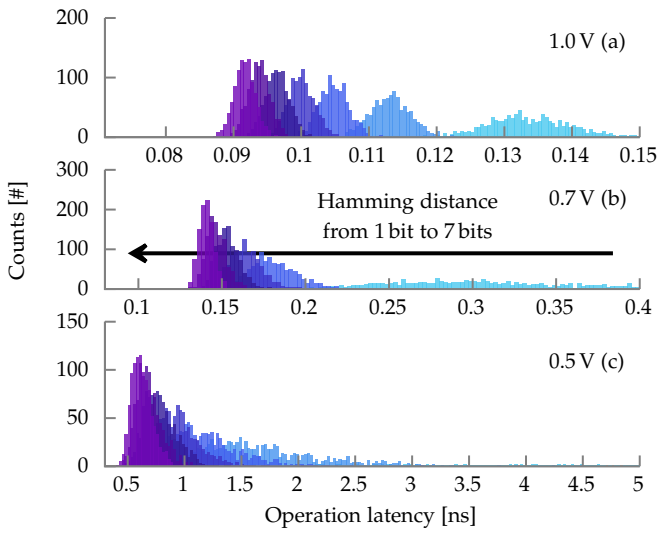


Fig. 12. The operation latencies of Fe-FinFET TCAM under process variation at three different supply voltages. The variation for one miss is particularly high at 0.5 V ranging from 0.8 ns to 5.0 ns (not recognizable in the plot). The block size is 15 bits. The results are based on 1000 Monte-Carlo SPICE simulations per voltage level and Hamming distance.

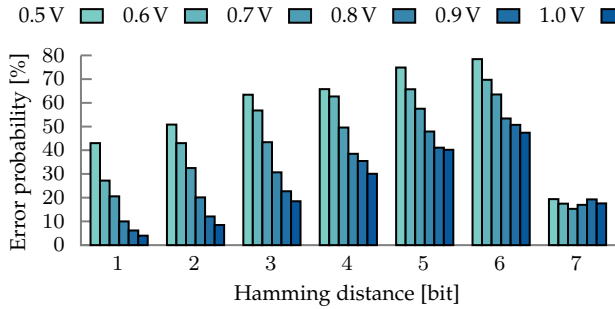


Fig. 13. Fe-FinFET TCAM error probabilities of the individual Hamming distances under process variation at different supply voltages V_{DD} . The results are based on 1000 Monte-Carlo SPICE simulations per voltage level and Hamming distance. The block size is 15 bits and the maximum detectable Hamming distance is seven bits.

Figure 13 shows that the higher process variation results in a higher error probability. Whereas SRAM peaked at 40 %, Fe-FinFET reaches 78 %. Interestingly, the observed trend from Figure 6 is not repeated. Instead, an increase in supply voltage proportionally decreases the error probability. The worse error probabilities translate further into higher inference accuracy losses. Although HDC is very robust against noise, such high error rates inevitably reduce the inference accuracy. Figure 14 shows this increased loss. For seven-bit block sizes, while in SRAM, the loss in inference accuracy can be limited to less than 0.05 % by using higher voltages, Fe-FinFET can achieve 0.3 % at best. For smaller block sizes, inference accuracy loss can be lower but not as low as with SRAM. Energy for a comparison operation is comparable between both technologies with a 19 % advantage for SRAM at 0.5 V and almost identical at 0.7 V and 1.0 V with $\pm 2 \%$.

6.3 Impact of Temperature

Previous work has investigated the impact of temperature on Fe-FinFET-based TCAM blocks [44]. They showed that

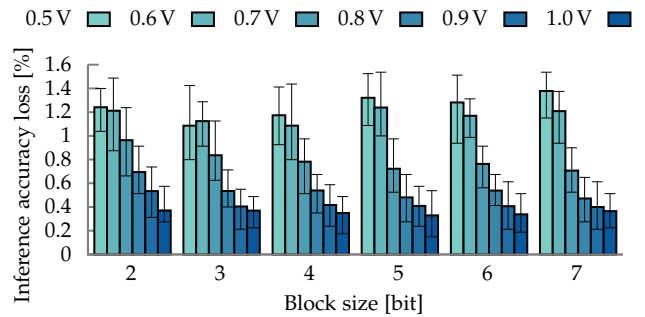


Fig. 14. Loss in inference accuracy due to process variation on Fe-FinFET TCAM for language recognition.

the impact of temperature on Fe-FinFET-based TCAM is non-intuitive and complex.

To explore its implications at system level, a temperature analysis for both SRAM-based and Fe-FinFET-based TCAM blocks is conducted. To stay consistent with the previous analyses, the following TCAM configuration is used. The nominal supply voltage is 0.7 V and three different temperatures are considered: 27 °C (baseline), 65 °C, and 85 °C. The temperatures are applied to the whole circuit, i.e., the CSRA is also affected by the temperature increase. In addition to the impact of temperature on the underlying FinFET transistor (i.e., reductions in the threshold voltage and carrier mobility), temperature does also degrade the ferroelectric parameters (i.e., remnant polarization P_r , coercive field E_c , and saturation polarization P_s).

The SPICE analysis captures both effects, the impact of temperature on the underlying FinFET transistor as well as on the ferroelectric layer. The transistor compact model BSIM-CMG (calibrated with the Intel 14 nm FinFET measurement data) captures the impact of temperature on the underlying FinFET transistor. The impact of temperature on the ferroelectric layer is additionally modeled by us using experimental data for the P-V loops at various temperatures. Further details can be found in [45].

The results are presented in Figure 15(a) for SRAM-based TCAM blocks for language recognition at 10,000 bit. For all evaluated block sizes, the inference accuracy loss is lower with higher temperatures. Two opposing effects are at play. On one hand, the temperature-induced increase in operation latency increases the margins between the mismatch groups. On the other hand, the impact of process variation increases, widening the mismatch groups. For SRAM-based TCAM blocks, the increase in operation latency is dominant and thus the error probability is reduced. However, this reduction has little impact because the baseline error probability is already high. In other words, most of the computed Hamming distances are slightly incorrect already and higher temperatures do not correct this significantly. Only in edge

TABLE 2
Figures of merit for a single SRAM and Fe-FinFET-based TCAM cell.

	SRAM	Fe-FinFET	Diff [%]
Transistors [#]	16	2	-800
$E_{mismatch}$ [fJ]	1.15	1.24	7
Latency [ns]	0.099	0.305	308

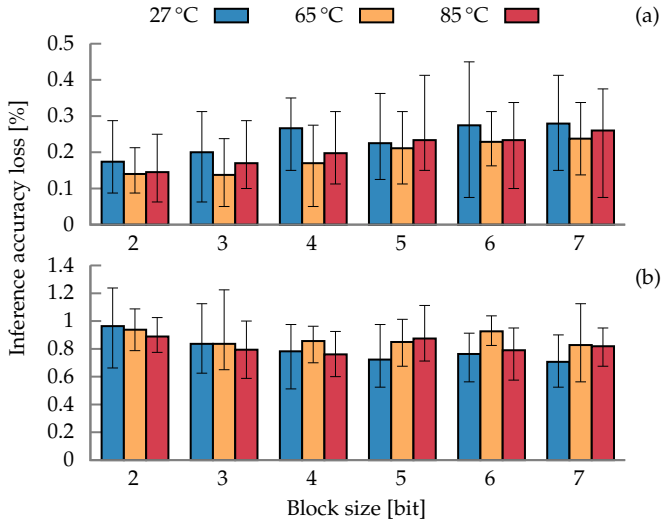


Fig. 15. Inference accuracy loss on (a) SRAM-based and (b) Fe-FinFET-based TCAM cells due to process variation. For language recognition using 10,000 bit, 0.7 V at different temperatures.

cases, where the error probability is not as high, is the impact of temperature measurable.

For Fe-FinFET-based TCAM blocks, it depends on the block size which effect has the higher impact as shown in Figure 15(b). For smaller block sizes up to 4 bit, a higher temperature reduces the loss in inference accuracy. With larger block sizes, the increased impact of process variation is higher and thus the loss increases. The initial investigation suggest possible tradeoffs and challenges at the system level. Further experiments and studies are required to explore the potentially positive impact of temperature in the inference accuracy.

6.4 Perspectives with Fe-FinFET TCAM

A comparison of the presented results for SRAM and Fe-FinFET underscores the maturity of the SRAM process. Further engineering work at the foundries has to reduce the level of process variation. Although Fe-FinFET TCAM-based HDC systems suffer higher accuracy losses, they still offer other benefits. Table 2 highlights the numeric differences. Most interestingly, only two Fe-FinFETs are necessary per TCAM cell. Even when considering the physical layout, a Fe-FinFET-based TCAM requires 13 % of an 16 transistor TCAM [43]. Thus, area-constrained HDC systems are possible that might otherwise be infeasible with SRAM. Given a limited area budget, an SRAM-based system might only fit 1000-bit vectors, whereas a Fe-FinFET-based system can fit 8000-bit vectors. This difference in vector length overcompensates the higher process variation. The Fe-FinFET-based system achieves a higher inference accuracy, although it consumes more energy for a comparison operation in the AM (see Figure 16). Nevertheless, the static power consumption in a Fe-FinFET-based system is much lower since it can be turned off due to its non-volatility. To evaluate those savings and compute the total energy consumption, the ratio of comparison operation to idle time has to be known, which highly depends on the target system.

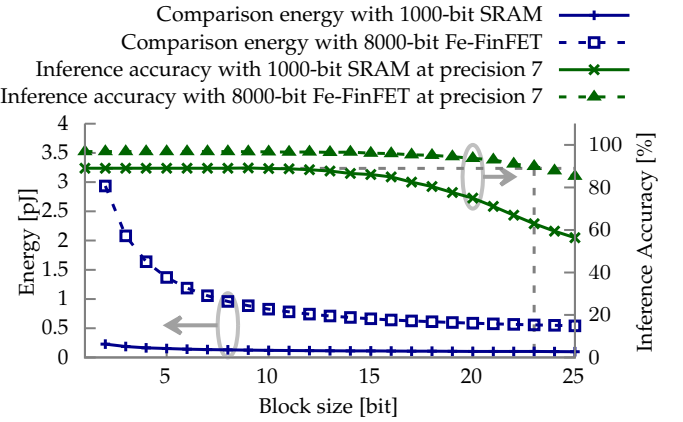


Fig. 16. With a restricted area budget, more Fe-FinFET-based TCAM cells are possible resulting in a higher inference accuracy despite the higher variability. At a block size of 23, the 8000-bit Fe-FinFET-based TCAM is as accurate as the SRAM baseline and consumes $5.5 \times$ more energy for a comparison of two vectors.

However, such a scheme does not scale if the area budget is sufficient to accommodate a large SRAM-based AM. As shown in Figure 2, increasing the vector length has diminishing returns. To still exploit the area savings, the Fe-FinFET-based arrays can be replicated multiple times. The query is applied to all arrays simultaneously, thus not increasing latency. Since all TCAM cells in each array are affected by process variation differently, the arrays can return different Hamming distances. The median distance is select, effectively ignoring the worst-affected and most inaccurate TCAM cells. In Figure 17, the benefits of this approach are shown. The given inference accuracy losses are averaged over all evaluated block sizes. With seven replicas, the loss in a Fe-FinFET-based system is on average 0.03 % higher than in a SRAM-based one. Such a difference is negligible because the random initialization of the vectors can have a bigger impact. With three or five replicas, the difference is limited to at most 0.26 % and 0.09 %, respectively. Compared to the Fe-FinFET baseline, three replicas already reduce the inference accuracy loss by up to 0.29 %. Further analyses have to be conducted to evaluate the increased power consumption.

In summary, for area or power-constrained systems, Fe-FinFET already offers an alternative to SRAM. If the area is not of concern, then Fe-FinFET-based TCAM arrays can be replicated to reduce the impact of variation. Advances in manufacturing technology and processes will also reduce this impact, leading to a more mature Fe-FinFET technology with better performance in HDC systems, among others.

7 CONCLUSION

In this work, we demonstrated that the resiliency of HDC against errors is larger than what has been previously assumed. We revealed the marginal impact of variability on the inference accuracy for SRAM-based TCAM cell and the role of applications. If a 0.5 % loss in inference accuracy is accepted, up to $11.5 \times$ energy saving would be possible in some applications. We also investigate the performance of Fe-FinFET-based TCAM cells and show the effect of process variation on such systems. Due to its prototype state, inference accuracy losses are higher but chip area and

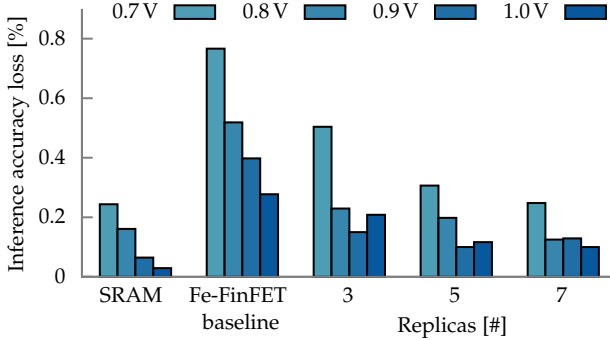


Fig. 17. Inference accuracy loss comparison of SRAM, Fe-FinFET baseline, and with Fe-FinFET replicas to reduce the impact of process variation. Results are averaged over block sizes from 2 to 7 bits.

static power can be reduced. Such gains can be traded off to counteract the effects of process variation. *All in all, HW/SW co-design is a key to achieve efficient, yet reliable in-memory hyperdimensional computing.*

ACKNOWLEDGEMENT

Authors thank X. Sharon Hu, Xunzhao Yin, and Kai Ni for their valuable support. This research was partially supported by Advantest as part of the Graduate School “Intelligent Methods for Test and Reliability” (GS-IMTR) at the University of Stuttgart and in part by the German Research Foundation (DFG) “ACROSS: Approximate Computing aCROss the System Stack”.

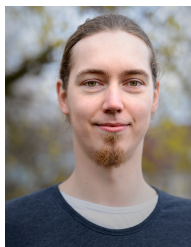
REFERENCES

- [1] V. Sze, Y.-H. Chen, T.-J. Yang, and J. S. Emer, “Efficient processing of deep neural networks: A tutorial and survey,” *Proceedings of the IEEE*, vol. 105, no. 12, pp. 2295–2329, 2017.
- [2] M. A. Hanif, F. Khalid, R. V. W. Putra, S. Rehman, and M. Shafique, “Robust machine learning systems: Reliability and security for deep neural networks,” in *2018 IEEE 24th International Symposium on On-Line Testing And Robust System Design (IOLTS)*, 2018, pp. 257–260.
- [3] A. Burrello, K. Schindler, L. Benini, and A. Rahimi, “One-shot learning for ieeg seizure detection using end-to-end binary operations: Local binary patterns with hyperdimensional computing,” in *2018 IEEE Biomedical Circuits and Systems Conference (BioCAS)*, 2018, pp. 1–4.
- [4] A. Rahimi, S. Benatti, P. Kanerva, L. Benini, and J. M. Rabaey, “Hyperdimensional biosignal processing: A case study for EMG-based hand gesture recognition,” in *2016 IEEE International Conference on Rebooting Computing (ICRC)*, Oct. 2016, pp. 1–8.
- [5] A. X. Manabat, C. R. Marcelo, A. L. Quinquito, and A. Alvarez, “Performance analysis of hyperdimensional computing for character recognition,” in *2019 International Symposium on Multimedia and Communication Technology (ISMAC)*, 2019, pp. 1–5.
- [6] G. Karunaratne, M. Le Gallo, G. Cherubini, L. Benini, A. Rahimi, and A. Sebastian, “In-memory hyperdimensional computing,” *Nature Electronics*, vol. 3, no. 6, pp. 327–337, Jun. 2020, number: 6 Publisher: Nature Publishing Group. [Online]. Available: <https://www.nature.com/articles/s41928-020-0410-3>
- [7] P. Kanerva, “Hyperdimensional Computing: An Introduction to Computing in Distributed Representation with High-Dimensional Random Vectors,” *Cognitive Computation*, vol. 1, no. 2, pp. 139–159, Jun. 2009. [Online]. Available: <http://link.springer.com/10.1007/s12559-009-9009-8>
- [8] T. F. Wu, H. Li, P.-C. Huang, A. Rahimi, J. M. Rabaey, H.-S. P. Wong, M. M. Shulaker, and S. Mitra, “Brain-inspired computing exploiting carbon nanotube FETs and resistive RAM: Hyperdimensional computing case study,” in *2018 IEEE International Solid - State Circuits Conference - (ISSCC)*. San Francisco, CA: IEEE, Feb. 2018, pp. 492–494. [Online]. Available: <http://ieeexplore.ieee.org/document/8310399/>
- [9] A. V. Khvalkovskiy, D. Apalkov, S. Watts, R. Chepulskii, R. S. Beach, A. Ong, X. Tang, A. Driskill-Smith, W. H. Butler, P. B. Visscher, D. Lottis, E. Chen, V. Nikitin, and M. Krounbi, “Basic principles of STT-MRAM cell operation in memory arrays,” *Journal of Physics D: Applied Physics*, vol. 46, no. 7, p. 074001, feb 2013. [Online]. Available: <https://iopscience.iop.org/article/10.1088/0022-3727/46/7/074001>
- [10] H. Akinaga and H. Shima, “Resistive random access memory (reram) based on metal oxides,” *Proceedings of the IEEE*, vol. 98, no. 12, pp. 2237–2251, Dec 2010.
- [11] S. Dünkel, M. Trentzsch, R. Richter, P. Moll, C. Fuchs, O. Gehring, M. Majer, S. Wittek, B. Müller, T. Melde, H. Mulaosmanovic, S. Slesazeck, S. Müller, J. Ocker, M. Noack, D. Löhr, P. Polakowski, J. Müller, T. Mikolajick, J. Höntschel et al., “A fetef based super-low-power ultra-fast embedded nvm technology for 22nm fdsOI and beyond,” in *2017 IEEE International Electron Devices Meeting (IEDM)*, Dec 2017, pp. 19.7.1–19.7.4.
- [12] D. Reis, K. Ni, W. Chakraborty, X. Yin, M. Trentzsch, S. Dünkel, T. Melde, J. Müller, S. Beyer, S. Datta, M. Niemier, and X. S. Hu, “Design and analysis of an ultra-dense, low-leakage and fast fetef-based random access memory array,” *IEEE Journal on Exploratory Solid-State Computational Devices and Circuits*, pp. 1–1, 2019.
- [13] J. Song, H. Dixit, B. Behin-Aein, C. H. Kim, and W. Taylor, “Impact of process variability on write error rate and read disturbance in stt-mram devices,” *IEEE Transactions on Magnetics*, vol. 56, no. 12, pp. 1–11, 2020.
- [14] G. Krishnan, J. Sun, J. Hazra, X. Du, M. Liehr, Z. Li, K. Beckmann, R. Joshi, N. C. Cady, and Y. Cao, “Robust rram-based in-memory computing in light of model stability,” in *2021 IEEE International Reliability Physics Symposium (IRPS)*, 2021, pp. 1–5.
- [15] K. Ni, A. Gupta, O. Prakash, S. Thomann, X. S. Hu, and H. Amrouch, “Impact of extrinsic variation sources on the device-to-device variation in ferroelectric fet,” in *2020 IEEE International Reliability Physics Symposium (IRPS)*, 2020, pp. 1–5.
- [16] M. Imani, A. Rahimi, D. Kong, T. Rosing, and J. M. Rabaey, “Exploring Hyperdimensional Associative Memory,” in *2017 IEEE International Symposium on High Performance Computer Architecture (HPCA)*, Feb. 2017, pp. 445–456, iSSN: 2378-203X.
- [17] K. Ni, X. Yin, A. F. Laguna, S. Joshi, S. Dünkel, M. Trentzsch, J. Müller, S. Beyer, M. Niemier, X. S. Hu, and S. Datta, “Ferroelectric ternary content-addressable memory for one-shot learning,” *Nature Electronics*, vol. 2, no. 11, pp. 521–529, 2019.
- [18] G. Karunaratne, M. Hersche, J. Langeneager, G. Cherubini, M. L. Gallo, U. Egger, K. Brew, S. Choi, I. Ok, C. Silvestre, N. Li, N. Saulnier, V. Chan, I. Ahsan, V. Narayanan, L. Benini, A. Sebastian, and A. Rahimi, “In-memory realization of in-situ few-shot continual learning with a dynamically evolving explicit memory,” in *ESSCIRC 2022- IEEE 48th European Solid State Circuits Conference (ESSCIRC)*, 2022, pp. 105–108.
- [19] A. Rahimi, P. Kanerva, and J. M. Rabaey, “A Robust and Energy-Efficient Classifier Using Brain-Inspired Hyperdimensional Computing,” in *Proceedings of the 2016 International Symposium on Low Power Electronics and Design - ISLPED '16*. San Francisco Airport, CA, USA: ACM Press, 2016, pp. 64–69. [Online]. Available: <http://dl.acm.org/citation.cfm?doid=2934583.2934624>
- [20] U. Quasthoff, M. Richter, and C. Biemann, “Corpus portal for search in monolingual corpora.” in *LREC*, 2006, pp. 1799–1802.
- [21] P. Koehn, “Europarl: A Parallel Corpus for Statistical Machine Translation,” in *Conference Proceedings: the tenth Machine Translation Summit*, AAMT. Phuket, Thailand: AAMT, 2005, pp. 79–86. [Online]. Available: <http://mt-archive.info/MTS-2005-Koehn.pdf>
- [22] F. Yang and S. Ren, “On the vulnerability of hyperdimensional computing-based classifiers to adversarial attacks,” in *International Conference on Network and System Security*. Springer, 2020, pp. 371–387.
- [23] P. R. Gensler, A. Vas, and H. Amrouch, “Brain-inspired hyperdimensional computing: How thermal-friendly for edge computing?” *IEEE Embedded Systems Letters*, 2022.
- [24] M. Imani, X. Yin, J. Messerly, S. Gupta, M. Niemier, X. S. Hu, and T. Rosing, “Searchd: A memory-centric hyperdimensional computing with stochastic training,” *IEEE Transactions on Computer-Aided Design of Integrated Circuits and Systems*, vol. 39, no. 10, pp. 2422–2433, 2020.
- [25] G. Karunaratne, M. Schmuck, M. Le Gallo, G. Cherubini, L. Benini, A. Sebastian, and A. Rahimi, “Robust high-dimensional memory-augmented neural networks,” *Nature communications*, vol. 12, no. 1, pp. 1–12, 2021.

- [26] A. Kazemi, M. M. Sharifi, A. F. Laguna, F. Müller, R. Rajaei, R. Olivo, T. Kämpfe, M. Niemier, and X. S. Hu, "In-memory nearest neighbor search with fefet multi-bit content-addressable memories," in *2021 Design, Automation & Test in Europe Conference & Exhibition (DATE)*, 2021, pp. 1084–1089.
- [27] Y. LeCun and C. Cortes, "MNIST handwritten digit database," 2010. [Online]. Available: <http://yann.lecun.com/exdb/mnist/>
- [28] A. Kazemi, M. M. Sharifi, Z. Zou, M. Niemier, X. S. Hu, and M. Imani, "Mimhd: Accurate and efficient hyperdimensional inference using multi-bit in-memory computing," in *2021 IEEE/ACM International Symposium on Low Power Electronics and Design (ISLPED)*, 2021, pp. 1–6.
- [29] R. Karam, R. Puri, S. Ghosh, and S. Bhunia, "Emerging trends in design and applications of memory-based computing and content-addressable memories," *Proceedings of the IEEE*, vol. 103, no. 8, pp. 1311–1330, 2015.
- [30] H.-J. Tsai, K.-H. Yang, Y.-C. Peng, C.-C. Lin, Y.-H. Tsao, M.-F. Chang, and T.-F. Chen, "Energy-efficient tcam search engine design using priority-decision in memory technology," *IEEE Transactions on Very Large Scale Integration (VLSI) Systems*, vol. 25, no. 3, pp. 962–973, 2017.
- [31] Y.-J. Chang, "A high-performance and energy-efficient tcam design for ip-address lookup," *IEEE TCAS-II*, vol. 56, no. 6, pp. 479–483, 2009.
- [32] S. Natarajan, M. Agostinelli, S. Akbar, M. Bost, A. Bowonder, V. Chikarmane, S. Chouksey, A. Dasgupta, K. Fischer, Q. Fu, T. Ghani, M. Giles, S. Govindaraju, R. Grover, W. Han, D. Hanken, E. Haralson, M. Haran, M. Heckscher, R. Heussner *et al.*, "A 14nm logic technology featuring 2nd-generation finfet, air-gapped interconnects, self-aligned double patterning and a 0.0588 μm^2 sram cell size," in *2014 IEEE International Electron Devices Meeting*, 2014, pp. 3.7.1–3.7.3.
- [33] J. P. Duarte, S. Khandelwal, A. Medury, C. Hu, P. Kushwaha, H. Agarwal, A. Dasgupta, and Y. S. Chauhan, "Bsim-cmg: Standard finfet compact model for advanced circuit design," in *Conference 2015 - 41st European Solid-State Circuits Conference (ESSCIRC)*, 2015, pp. 196–201.
- [34] S. Lobov, N. Krilova, I. Kastalskiy, V. Kazantsev, and V. A. Makarov, "Latent Factors Limiting the Performance of sEMG-Interfaces," vol. 18, no. 4, p. 1122.
- [35] D. Dua and C. Graff, "UCI machine learning repository." [Online]. Available: <http://archive.ics.uci.edu/ml>
- [36] D. Reis, M. Niemier, and X. S. Hu, "A computing-in-memory engine for searching on homomorphically encrypted data," *IEEE Journal on Exploratory Solid-State Computational Devices and Circuits*, pp. 1–1, 2019.
- [37] J. G. Alzate, U. Arslan, P. Bai, J. Brockman, Y. J. Chen, N. Das, K. Fischer, T. Ghani, P. Heil, P. Hentges, R. Jahan, A. Littlejohn, M. Mainuddin, D. Ouellette, J. Pellegren, T. Pramanik, C. Puls, P. Quintero, T. Rahman, M. Sekhar *et al.*, "2 mb array-level demonstration of stt-mram process and performance towards 14 cache applications," in *2019 IEEE International Electron Devices Meeting (IEDM)*, Dec 2019, pp. 2.4.1–2.4.4.
- [38] S. Mueller, "Ferroelectric hfo₂ and its impact on the memory landscape," in *2018 IEEE International Memory Workshop (IMW)*, May 2018, pp. 1–4.
- [39] M. T. Bohr, R. S. Chau, T. Ghani, and K. Mistry, "The high-k solution," *IEEE Spectrum*, vol. 44, no. 10, pp. 29–35, Oct 2007.
- [40] S. Beyer, S. Dünkel, M. Trentzsch, J. Müller, A. Hellmich, D. Utess, J. Paul, D. Kleimaier, J. Pellerin, S. Müller, J. Ocker, A. Benoit, H. Zhou, M. Mennenga, M. Schuster, F. Tassan, M. Noack, A. Pourkeramati, F. Müller, M. Lederer *et al.*, "Fefet: A versatile cmos compatible device with game-changing potential," in *2020 IEEE International Memory Workshop (IMW)*, 2020, pp. 1–4.
- [41] T. Mikolajick, S. Slesazeck, M. H. Park, and U. Schroeder, "Ferroelectric hafnium oxide for ferroelectric random-access memories and ferroelectric field-effect transistors," *MRS Bulletin*, vol. 43, no. 5, p. 340–346, 2018.
- [42] W. Banerjee, I. V. Karpov, A. Agrawal, S. Kim, S. Lee, S. Lee, D. Lee, and H. Hwang, "Highly-stable (< 3% fluctuation) ag-based threshold switch with extreme-low off current of 0.1 pa, extreme-high selectivity of 10⁹ and high endurance of 10⁹ cycles," in *2020 IEEE International Electron Devices Meeting (IEDM)*, 2020, pp. 28.4.1–28.4.4.
- [43] X. Yin, K. Ni, D. Reis, S. Datta, M. Niemier, and X. S. Hu, "An Ultra-Dense 2FeFET TCAM Design Based on a Multi-Domain FeFET Model," *IEEE Transactions on Circuits and Systems II: Express Briefs*, vol. 66, no. 9, pp. 1577–1581, Sep. 2019, conference Name: IEEE Transactions on Circuits and Systems II: Express Briefs.
- [44] S. Thomann, C. Li, C. Zhuo, O. Prakash, X. Yin, X. S. Hu, and H. Amrouch, "On the reliability of in-memory computing: Impact of temperature on ferroelectric tcam," in *2021 IEEE 39th VLSI Test Symposium (VTS)*, 2021, pp. 1–6.
- [45] A. Gupta, K. Ni, O. Prakash, X. S. Hu, and H. Amrouch, "Temperature Dependence and Temperature-Aware Sensing in Ferroelectric FET," in *2020 IEEE International Reliability Physics Symposium (IRPS)*, Apr. 2020, pp. 1–5, iSSN: 1938-1891.



Simon Thomann (M'22) earned his degrees in Computer Science, Master ('22) as well as Bachelor ('19), at Karlsruhe Institute of Technology (KIT), Germany. He is currently pursuing his Ph.D. at the Chair of Semiconductor Test and Reliability (STAR) at the University of Stuttgart. His research interests range from device to system level. His Special interest lies in circuit design, emerging technologies, and cross-layer reliability modeling from device to circuit level. ORCID 0000-0002-7902-9353



Paul R. Gessler (M'21) received the Dipl. Inf degree (M.Sc.) in computer science in 2017 at TU Dresden, Germany. In 2018 he started his PhD research at the Chair for Embedded Systems (CES) at Karlsruhe Institute of Technology, Germany. Since 2020 he continues his PhD at the Semiconductor Test and Reliability (STAR) chair within the Computer Science, Electrical Engineering Faculty at the University of Stuttgart. His research interests include emerging technologies, system architecture, and emerging brain-inspired methods for IC test and beyond. ORCID 0000-0002-7175-7284



Hussam Amrouch (S'11-M'15) is a Junior Professor heading the Chair of Semiconductor Test and Reliability (STAR) within the Computer Science, Electrical Engineering Faculty at the University of Stuttgart. He received his Ph.D. degree with distinction (*Summa cum laude*) from the Karlsruhe Institute of Technology in 2015. He holds seven HiPEAC Paper Awards and three best paper nominations at top EDA conferences: DAC'16, DAC'17 and DATE'17 for his work on reliability. He has 200+ publications in multidisciplinary research areas, starting from semiconductor physics to circuit design all the way up to CAD and computer architecture. Jun.-Prof. Amrouch has delivered 9 tutorial talks in major EDA conferences like DAC and DATE and 25 invited talks (including 2 Keynotes) in several international conferences, universities, and companies. ORCID 0000-0002-5649-3102.